Journal of Metals, Materials and Minerals, 34(3), 1861, 2024

Effect of hatch spacing in selective laser melting process of Ti-6Al-4V alloy on finished surface roughness: A computational study

Reettiporn THONGPRON[1], Patiparn NINPETCH[2], Prasert CHALERMKARNNON[3], and Pruet KOWITWARANGKUL[1,*]

[1] *The Sirindhorn International Thai-German Graduate School of Engineering (TGGS), King Mongkut's University of Technology North Bangkok, Bangkok 10800, Thailand*

[2] *Department of Industrial Engineering, Faculty of Engineering, Rajamangala University of Technology Thanyaburi, Pathum Thani, 12110, Thailand*

[3] *Assistive Technology and Medical Devices Research Center, National Science and Technology Development Agency, Pathum Thani 12120, Thailand*

***Corresponding author e-mail**: pruet.k@tggs.kmutnb.ac.th

Received date:
30 September 2023
Revised date:
29 January 2024
Accepted date:
28 May 2024

Keywords:
Selective laser melting;
Overlap;
Multi-tracks;
CFD simulation;
Ti-6Al-4V

Abstract

The Selective Laser Melting (SLM) process is a promising additive manufacturing technology for producing complex metal parts. However, this process has certain limitations, including lack of fusion and defects, which can hinder its industrial applications. These challenges can be addressed by determining the appropriate overlap percentage parameters. This study used numerical simulation to explore the effect of overlap percentage on multi-track melting in the SLM process for Ti-6Al-4V. The simulation results categorize the multi-track melting morphologies into two distinct groups. The first group, (0% to 40% overlap), displays consistent surface roughness with an average Ra value of 7 μm. In contrast, the second group (50% to 60% overlap), shows non-uniform shapes. Specifically, the three central tracks in this group present an Ra value of approximately 4 μm. However, when all five tracks of this group are taken into account, the average Ra rises to 14 μm. These differences in surface roughness can be attributed to factors like energy density and the Marangoni effect. Both melt pool depth and shrinkage depth in the overlap area are significant as they might contribute to the risk of the lack of fusion defects. The insights from this research hold potential in shaping scanning pattern strategy design.

1. Introduction

Selective Laser Melting (SLM) process is a typical layer-based method in metal additive manufacturing (MAM). In the SLM process, the laser source with high power is employed as a moving heat energy for melting metal powders for fabricating metallic parts with complex geometries [1]. The SLM process finds widespread applications in various industries, including automotive, aerospace, and medical fields [2]. The SLM process generally involves many physical phenomena, particularly heat transfer, phase transformation and molten fluid flow [3]. Nevertheless, these phenomena take place rapidly in a small area, resulting in in-situ experiments that are difficult for observation. Therefore, simulation modeling is an essential tool for observing and explaining the formation of physical phenomena throughout the SLM process and for investigating the impact of processing parameters on forming quality [4].

Many researchers are implementing numerical simulations to study heat transfer and fluid flow during the SLM process across a variety of materials. They especially focus on single-track laser melting models, considering process parameters such as laser power, scanning speed, and layer thickness [5-12]. Additionally, some researchers extend their simulations to multi-track and multi-layer SLM processes to investigate further process parameters, including scanning patterns and hatch spacing. All these details are provided in Table 1 [13-16].

In addition, the simulation modeling procedure typically begins with a validation process using experimental data in a single-track melting simulation. The process parameters, including, laser power, scanning speed, and layer thickness from the experimental data are necessary to ensure the model's reliability [17].

The multi-track melting in each layer or multi-layer was developed from the single-track melting with more variation of process parameters in multi-track such as hatch spacing and scanning pattern. These parameters have significant effects on the surface quality and defect of porosities, which are the main disadvantages of SLM process fabrication [18]. These defects are the main challenge to achieve the desired surface quality and fully dense finished parts [19]. Previous research studies have found alternative ways to improve the surface quality with the finishing process including mechanical, chemical, and thermal processes [20]. In addition, some researchers [18,21] used the Ra and Rz roughness values to indicate the improvement of the surface roughness.

Table 1. List of single-track and multi-track SLM simulation research works.

Journal	Materials	Simulation type
[5], [6], [7], [8]	Ti-6Al-4V	single-track melting
[9], [10]	SS 316L	

Therefore, this research aims to investigate the influence of hatch spacing parameter in terms of overlapping percentage which is indicated by using Volume Energy Density (VED) to compare the different VED values effects on the surface roughness and melt pool formation including melt pool depth and overlap depth in multi-tracks SLM. This study focuses on medical-grade Ti-6Al-4V titanium alloy, utilized as metal powder and solid substrates, extensively used in medical devices like orthopedic and dental implants due to its biomechanical properties, such as elasticity and fatigue strength, mirroring human bone. Ti-6Al-4V's excellent corrosion resistance ensures the long-term durability of implants in the human body. It is also biocompatible, lightweight, and offers superior strength-to-weight ratio compared to other alloys. [22,23].

The findings of this study can help to enhance the surface quality which is related to the porosity reduction and nearly full dense of finished parts. This method can also reduce the number of finishing processes and increase the productivity of the SLM process

2. Numerical setup

2.1 Powder bed generation model

The powder bed generation model is based on the principles of particle movement and particle contact, using the Discrete Element Method (DEM) to describe the movement in linear and angular momentum [24].

The DEM is a numerical technique used to calculate the individual particle velocities in the x, y, and z directions, encompassing both translational and angular movement of the particles, in accordance with Newton's second law of motion. Figure 1. illustrates the particle-to-particle force model used in DEM simulations. The contact forces between particles are determined by Equations (1-3).

Particle interaction force in normal direction:

$$\mathbf{F_{n\,i}} = -k_s\, dl\mathbf{n} - \eta_n\,(\mathbf{u}'\cdot\mathbf{n})\mathbf{n} \qquad (1)$$

Particle interaction force in tangential direction:

$$\mathbf{F_{t\,i}} = -\eta_t\,(\mathbf{u}' - (\mathbf{u}'\cdot\mathbf{n})\mathbf{n}) \qquad (2)$$

Total particle interaction force:

$$l_0 = r_i + r_j;\ l = \mathbf{x_j} - \mathbf{x_i};\ dl = l_0 - l;\ \mathbf{n} = \frac{1}{l};\ \mathbf{u}' = \mathbf{u_j} - \mathbf{u_i} \qquad (3)$$

where x_i is a coordinate vector of the center of individual particle-i, r_i is the particle radius, k_s is spring constant, m_i is particle mass, u_i is particle velocity vector, η is the drag coefficient.

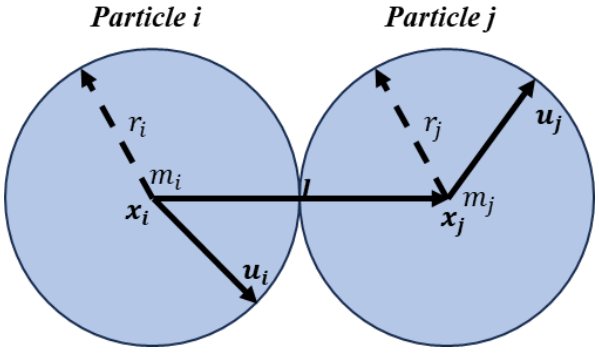

Figure 1. Particle-to-particle force model by DEM.

2.2 Thermo-fluid model

Many complex physics such as heat transfer, fluid dynamics and other phenomena are involved in the SLM process. These phenomena can be solved using the governing equations of mass, energy, and momentum as expressed in Equations (4) shows the mass conservation in SLM process [25,26]:

$$\frac{\partial \rho}{\partial t} + \nabla\,.\,(\rho\vec{v}) = 0 \qquad (4)$$

where $\vec{v}$ is the velocity of liquid metal, ρ is the metal density,

Due to thermal expansion induced non-uniform density the density distribution of molten pool, it is crucial to consider the buoyancy effects. Therefore, the momentum conservation equation is as follows [26]:

$$\frac{\partial \vec{v}}{\partial t} + \vec{v}.\nabla\vec{v} = \frac{1}{\rho}.\left(\mu\nabla^2 - \nabla p\vec{v}\right) + \vec{g} + \overrightarrow{F_B} \qquad (5)$$

where μ is the viscosity, p is pressure, t is time, $\vec{g}$ is gravity. $\overrightarrow{F_B}$ is the buoyancy force, which is calculated and described by Equation (6) [26]:

$$\overrightarrow{F_B} = \vec{g}\beta(T - T_m) \qquad (6)$$

where β is the thermal expansion coefficient, T is temperature, T_m is the liquidus temperature.

The surface tension in materials becomes particularly relevant when metal powder transforms into a liquid phase on the top surface. This change in surface tension is a consequence of heat and mass transfer within the melting area and can result in the occurrence of the phenomenon termed "Marangoni effects," which involves high thermal gradients. The surface tension is defined by Equation (7).

$$\gamma(T) = \gamma_0 + \frac{dy}{dT}(T - T_m) \qquad (7)$$

where γ is the surface tension at temperature, γ_0 is the surface tension at melting temperature, T_m is melting temperature, and $\frac{d\gamma}{dT}$ is the surface tension coefficient with temperature dependent.

The Volume of Fluid (VOF) model, a computational method, is employed to accurately capture and represent the surface morphology of the melt track during the SLM process [26], as demonstrated in Equation (8):

$$\frac{\partial F}{\partial t} + \nabla.\left(\vec{vF}\right) = 0 \quad (8)$$

The energy conservation equation is represented in Equation (9) [26]. The enthalpy (H) shown in Equation (9) is employed to account for the phase transformation phenomenon occurring between the solid and liquid phases during the SLM process. Additionally, the recoil pressure is utilized to describe the fluid flow phenomena of molten metal at the surface of the molten region when the temperature at the molten pool surface exceeds the boiling point of material. The recoil pressure is defined by Equation (10) [27,28].

$$\frac{\partial H}{\partial t} + (\vec{v}.\nabla)H = \frac{1}{\rho}.(\nabla.k\nabla T) + Q_{laser} \quad (9)$$

$$P_r = 0.54 P_0 exp\left(\Delta H_v \frac{T-T_b}{RTT_b}\right) \quad (10)$$

Where P_0 is the saturation pressure, R is gas constant and T_b is the boiling temperature of material.

2.3 Laser heat source model

In this study, the laser heat source model was characterized by a Gaussian distribution, is employed as the moving laser heat source above the metal particle bed. The laser heat source model is as follows [29]:

$$Q_{laser} = \frac{\eta P_{Laser}}{\pi D_S} exp\left(-2\frac{(x-x_s)^2+(y-y_s)^2}{D_s^2}\right) \quad (11)$$

Where Q_{laser} is the laser power, η is the absorption coefficient, P_{Laser} is the laser power, D_s is the laser diameter, x_s and y_s are the center coordinates of the laser beam.

2.4 Material properties

The material properties of Ti-6Al-4V alloys employed in the numerical simulation are shown in Table 2 [30]. Meanwhile, the thermal-physical properties with temperature dependent, including density, thermal conductivity, and specific heat are obtained from [31].

2.5 Computational configuration and processing parameters

The computational model setup starts with the generation of the powder bed using FLOW-DEM software to create a CAD file for the metal powder. Subsequently, the CAD file representing the geometry of metal powder is imported into the CFD simulation software FLOW-AM to simulate various aspects, including temperature distribution, molten pool dynamics, and multi-tracks melting. The computational domain for both single-track and multi-track melting processes is depicted in Figure 2. It should be noted that for an accurate representation of heat distribution similar to actual processing conditions, the domain would require significantly greater length and width than the current domain size. However, due to computational resource constraints, the model employs a simplified domain size. The element size within the melting area is set to 5 µm, while it is 8 µm for coverage over the substrate and the surrounding atmosphere.

A metal powder, comprising particles with diameters ranging from 12 µm to 31 µm, was deposited onto solid substrates measuring 1,200 µm × 2,000 µm × 300 µm (width × length × height). The layer thickness of the powder bed was set at 60 µm. Within the computational domain, specific boundary conditions were applied to control heat transfer. These conditions included convection and radiation exclusively on the top surface. Additionally, atmospheric pressure was set at the upper boundary. In this work, the simulation of single-track melting was firstly modeled to validate with experiment results from previous work of Kouprianoff *et al.* [33]. Then, simulation of multi-tracks melting was performed to examine the influence of the overlap percentage parameter. The number of multi-track melting for the study are five tracks. Moreover, the volumetric energy density (VED) in the study ranges from 22 J·mm^{-3} to 50 J·mm^{-3}. The laser power and scanning speed are set at 170 W and 1200 mm·s^{-1}, respectively. The VED is defined as the ratio of laser power (P) to the product of scanning speed (v), hatch spacing (h), and layer thickness (Lt), as illustrated in Equation (12).

$$VED = \frac{Laserpower\ (P)}{Scanningspeed\ (v) \times Layerthickness\ (L_t) \times Hatchspacing\ (h)} \quad (12)$$

2.6 Overlap percentage, melt track depth and overlap depth

This study aims to study the influence of hatch spacing parameter which represents an overlap percentage that effects on the quality of melting tracks listed in Table 3, in this study defined as bi-directional scanning pattern with different overlap percentage from 10% to 60% respectively.

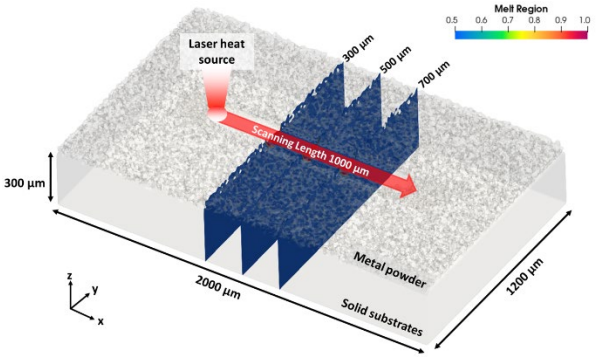

Figure 2. The computational domain for both single-track and multi-track melting process.

Table 2. Material properties used in the simulation [31].

Material properties	Value
Solidus temperature	1877 K
Liquidus temperature	1933 K
Boiling temperature	3533 K
Latent heat of melting	3.5×10^5 J·kg^{-1}
Latent heat of evaporation	7.34×10^6 J·kg^{-1}

Table 3. Process parameters for the present study.

Overlap percentage (%)	Hatch spacing (µm)	VED (J·mm^{-3})
10	106	24
20	94	27
30	83	30
40	71	35
50	59	42
60	47	53

The schematic of the melt pool with the parameters in (a) single – track melting and (b) multi – tracks melting in cross section view was illustrated in Figure 3.

$$overlap(\%) = \left(\frac{w-h}{w}\right) \times 100 \quad (13)$$

where w is the melt pool width, d is the melt pool depth which is measured from the surface substrate to the bottom of melt pool, $d_{overlap}$ is the melt pool depth in overlap zone, h is the hatch spacing parameter, Sh is the shrinkage distance and $Sh_{overlap}$ is the shrinkage distance in overlap zone which are measured from the height of the layer thickness of 60 µm as the reference. The overlap percentage was calculated by using this equation with the parameters of width, **w** and hatch spacing, h.

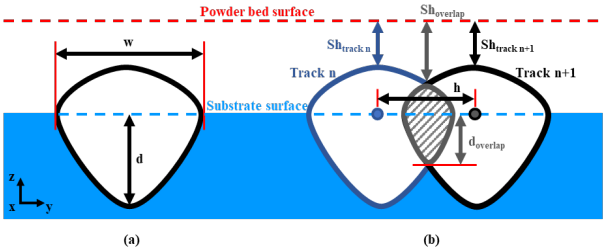

Figure 3. schematic of melt pool in cross section view with parameters (a) single – track melting and (b) multi – track melting.

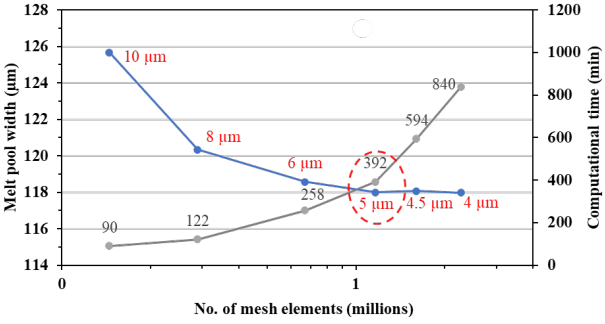

Figure 4. Mesh convergence analysis.

2.7 Mesh convergence analysis

Mesh convergence analysis stands as a crucial step in ensuring the model's reliability, and it was undertaken to determine the optimal mesh size for this study. Mesh sizes ranging from 10, 8, 6, 5, 4.5, to 4 µm were employed, corresponding to total mesh counts of 0.15, 0.29, 0.67, 1.16, 1.61 and 2.28 million elements, respectively. The mesh convergence analysis centered on the melt pool width in single-track melting were illustrated in Figure 4. The results revealed that the melt pool width converged as the mesh size reduced to 5 µm. However, further reduction in mesh size below 5 µm resulted in a significant increase in computational time. Taking both mesh convergence and computational efficiency into account, a mesh size of 5 µm was chosen for the numerical simulations in this study.

3. Results and discussion

3.1 Model validation in single – track melting

In this study, the model validation was conducted by comparing the numerical and experimental results of melt pool shape from Kouprianoff *et al*. [33]. The L-PBF machine of EOSINT M280, with a building platform of 250 mm × 250 mm, was used to build the experimental parts. Figure 5(a) shows the experiment results of melt pool shape with the scale bar. Figure 5(b) displays the melt pool shape with the color bar of the melt region from unmelt region in blue to melted region in red.

The numerical results were averaged from three different cross-sectional views at 300 µm, 500 µm, and 700 µm of the melt track length along the x–axis as illustrated in Figure 2. The average numerical results of melt pool width and depth equal to 118 µm and 35.4 µm, whereas the experiment results of melt pool width and depth around 115 µm and 35 µm respectively. The comparison of width and depth between the numerical results and experimental results demonstrated that the simulation model yields minor differences of less than 3% when compared with the experimental results. These findings indicated the reliability of the simulation model and its applicability to this study.

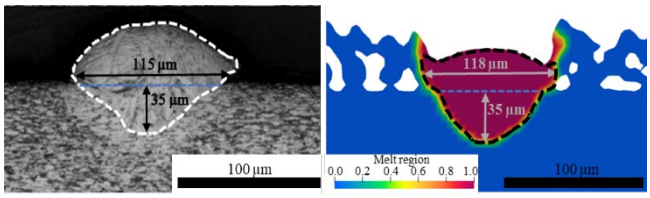

Figure 5. Comparing melt pool shape in cross-sectional view between (a) experimental results from Kouprianoff et al. [33], and (b) numerical results.

3.2 Temperature distribution and melt pool formation

Figure 6 displays the simulation results for temperature distribution on the metal powder and melt pool formation, presenting top view for a 10% overlap percentage. The temperature distribution of the powder bed is represented by a color contour. The results reveal that at 830 µs, Figure 6(a) shows the melting temperature of the melt track continuing above the liquidus temperature at the end of the first track. Figure 6(b) illustrates the scenario at time 1660 µs, where the laser continues moving from the first to the second melting track, following a bi-directional scanning pattern and overlapping with some area of the first track. By 2490 µs, as seen in Figure 6(c), the solidification time of the melting track is longer than the previous track, resulting in a longer temperature contour above liquidus temperature on melting track due to the heat accumulation in the powder bed. The laser source continues moving, reaching the end of the fourth and fifth tracks at times 3320 µs and 4150 µs, respectively, as depicted in Figures 6(d-e). The simulation concludes at 5000 µs, with five melting tracks undergoing cooling until they reach a temperature below the solidus, resulting in the formation of solidified tracks as shown in Figure 6(f).

Moreover, during the solidification process, the first track is surrounded by metal powders on both sides, leading to a symmetric temperature distribution, as shown in Figure 6(a). In contrast, the temperature distribution in the subsequent second, third, fourth, and fifth tracks is asymmetric. This asymmetry arises because, during solidification, one side is bordered by a previously solidified track, and the other side by metal powders, which possess lower thermal conductivity than the solid layer (refer to Figures 6(b-d), and Figure(f)). Additionally, the formation of evaporation recoil pressure on the molten pool's surface—when the molten metal exceeds its boiling point—causes the surface to depress under laser beam irradiation. As depicted in Figure 6(a), this results in a continuous and smooth morphology for the first solidified track. After completing the first track, the laser heat source moves in the opposite direction to form the second track. During the scanning of the second track, the molten metal from this track can merge with that of the first, leading to an expansion of the molten pool in the second track, as observed in Figure 6(b). This expansion is attributed to the reversal of the molten metal flow from the first track, driven by the intense centrifugal motion induced by the Marangoni effect in the second track. The flow dynamics within the molten pool for the third, fourth, and fifth tracks demonstrate similar characteristics, as illustrated in Figures 6(c), (d), and (f).

Additionally, the multi-track melting simulation model was evaluated by matching the outcomes from the current simulation upon the completion of the second track with those from Chen *et al.* [34], which encompass both numerical and experimental findings. Chen *et al.* utilized parameters such as a laser power of 250 W, scanning speed of 600 mm·s^{-1}, hatch spacing of 60 µm, and layer thickness of 50 µm. In contrast, this study used a laser power of 170 W, scanning speed of 1200 mm·s^{-1}, hatch spacing of 59 µm, and layer thickness of 30 µm. The melt track widths were measured at 166 µm in Chen *et al.*'s study and 179 µm in the current analysis. The wider melt track width in this study can be attributed to the bi-directional scanning pattern, which maintains a continuous moving heat source for the next track. Conversely, Chen *et al.* employed a unidirectional pattern, which involves pausing the moving heat source while transitioning to the next track.

The temperature tracking results, depicted in Figure 7, were collected using a temperature probe positioned at the center of the third melting track. Figure 7 illustrates these results, with different colored lines on the graph representing various case studies ranging from 10 to 60 percent overlap. At lower overlap percentages, the temperature exceeds the liquidus line only when the laser passes over the probe in the third track. However, at higher overlaps of 50 percent or more, the temperature consistently remains above the liquidus line. This behavior suggests that the metal powder starts melting as the laser moves through the second track, undergoes remelting within the third track, and experiences further remelting after the laser traverses the fourth track. These observed phenomena can significantly influence the evolution of the fabricated parts.

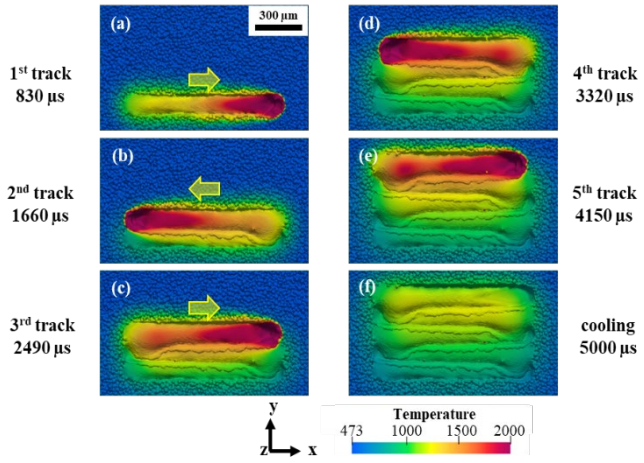

Figure 6. The simulation results of temperature distribution on the metal powder and melt pool formation from a top view in case of 10 percent overlap.

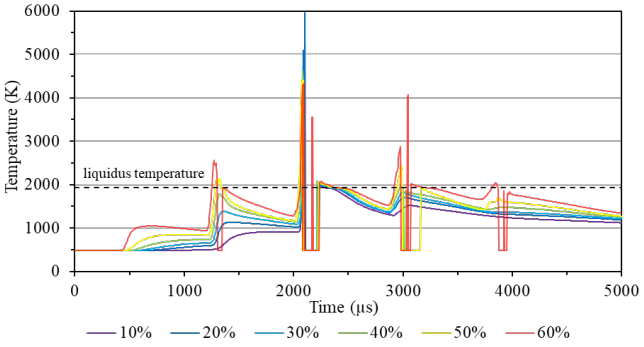

Figure 7. Temperature profile of the probe at middle of third track on different case studies.

3.3 Influence of overlap percentage effects on surface roughness

Figure 8 illustrates the simulation results for the surface morphology of multiple melting tracks and the formation of the melt pool, as viewed from the top. According to the simulation results, the surface morphology of the multi-track melting can be categorized into two groups. The first group, with overlap percentages ranging from 0% to 40%, exhibits uniform melt pool surface morphologies in terms of shape and melt track height across each track. Conversely, the second group, with overlap percentages exceeding 50%, displays notable differences in surface morphology, with non-uniform melt pool shapes and heights, especially in the case of 60% overlap. These phenomena are influenced by the effects of energy density and the Marangoni effect, induced by surface tension gradients.

Moreover, the surface morphology of the melting track, under varying overlap percentages, can impact the surface roughness, denoted as Ra. The Ra value of the first group, measured across five melting tracks, is around 7 µm, with the VED ranging from 24 J·mm^{-3} to 35 J·mm^{-3}. Notably, the three middle melting tracks within this group displayed a similar average Ra value of approximately 6 µm. In contrast, the second group, which consists of cases with overlap percentages of 50% and 60%, exhibited notably higher Ra values, averaging around 14 µm with the VED ranging from 42 J·mm^{-3} to 53 J·mm^{-3}. Upon closer examination of three melting tracks in this group, excluding the initial and final tracks, a significantly lower average Ra value of approximately 4 µm was observed. It is crucial to note that cases in the first group with a 10% overlap percentage exhibited certain issues, such as un-melted powder and spatter, making them more susceptible to defects. The surface roughness, Ra, for each case is listed in Table 4.

3.4 Influence of overlap percentage effects on melt pool depth and overlap depth

The measurements presented in Figure 3 were taken from the surface of the substrates and serve as a reference point to determine both the depth and shrinkage of the melt pool on each track. The term 'melt pool depth' is used to describe this depth measurement, while the measurement between tracks is termed the 'melt pool overlap depth.' Similarly, 'shrinkage depth' refers to the shrinkage measurement, and the measurement between tracks is called the 'shrinkage overlap depth.' The results for melt pool depth, overlap depth, shrinkage depth, and shrinkage overlap depth, visualized in Figure 8 from a cross-section view, are plotted as shown in Figure 9 and Figure 10.

In the first three cases, the depths of the five melting tracks have overlapping percentages ranging from 10% to 30%, resulting in minor variations in depth. However, for cases with overlap percentages ranging from 40% to 60%, especially in the last track, a significant increase in melt track depth is observed. This phenomenon can be attributed to the adoption of higher overlap percentages, which leads to increased heat accumulation within the melt tracks during the process, as illustrated in Figure 9(a). Furthermore, as the overlap percentage escalates from 10% in the initial case to 60% in subsequent cases, a gradual and linear increase in the overlap depth is noticeable. These trends are clearly depicted in the results shown in Figure 9(b).

In Figure 10(a), it is observed that for the first track, the shrinkage depth increases with the rise in overlap. From the second to the fourth track, the shrinkage depth experiences a more significant increase, particularly when the overlap reaches 50% and 60%. However, for the fifth track, the shrinkage depth decreases as the overlap increases. In Figure 10(b), a slight increase in shrinkage overlap depth is noted with the rise in overlap.

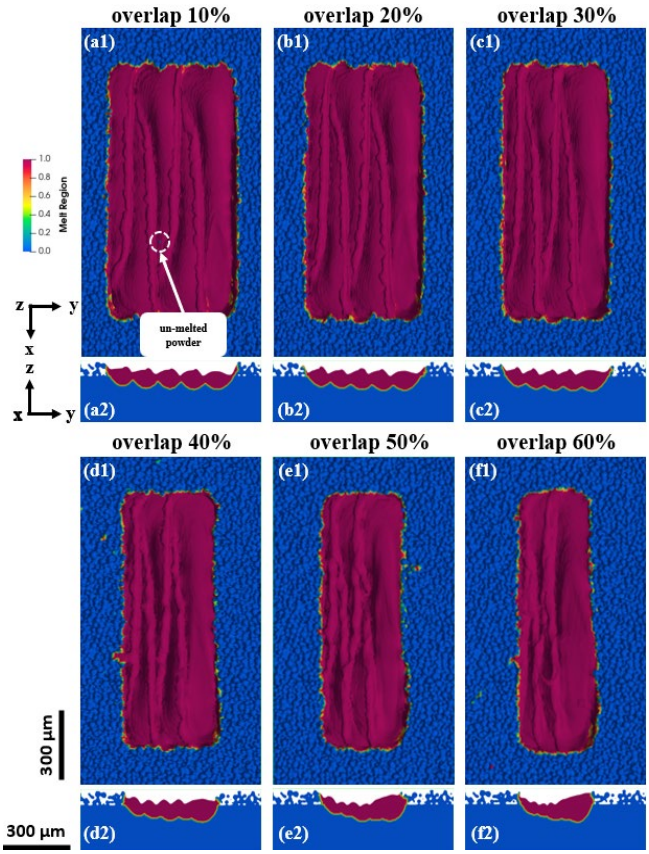

Figure 8. Examples of surface morphology in top view and melt track formation in cross-section view at finish time.

Table 4. Surface roughness, R_a at half-track length.

Case overlap (%)	R_a of 5 tracks (µm)	R_a of 3 tracks (µm)
0	6.5	6.6
10	7.7	6.7
20	6.6	6.7
30	6.1	6.3
40	6.5	6.1
50	14.3	4.5
60	14.4	3.4

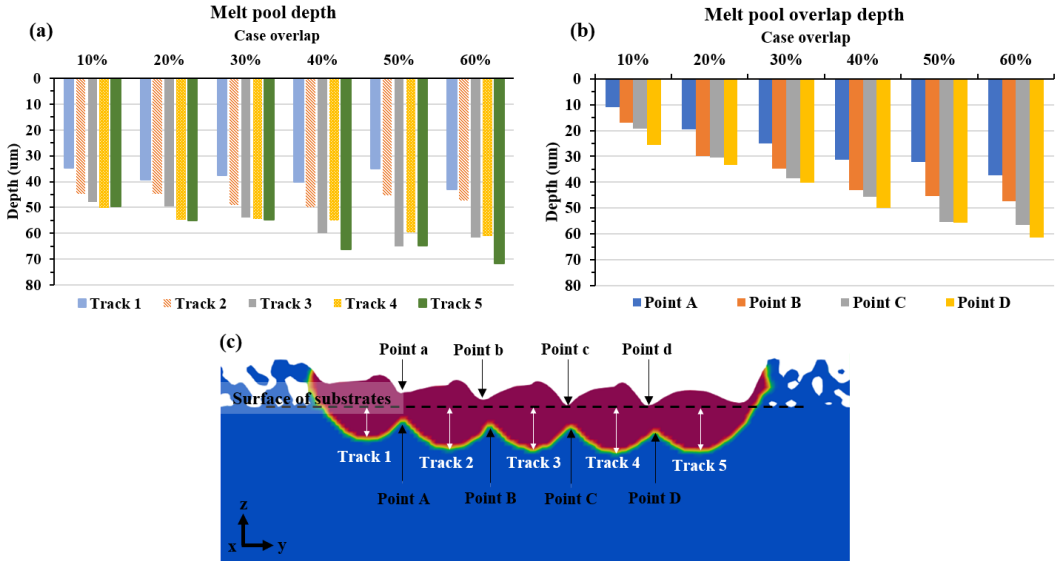

Figure 9. (a) Melt pool depth, (b) Melt pool overlap depth, (c) reference points for melt pool overlap depth (Point A-D) and shrinkage overlap depth (Point a-d) of six simulation cases.

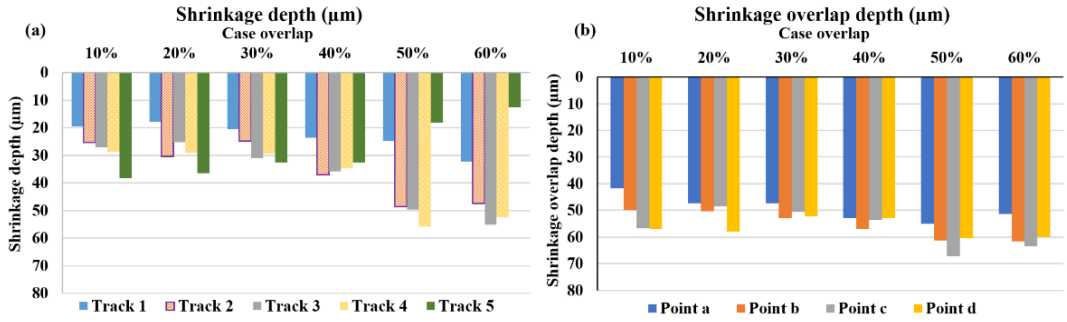

Figure 10. (a) Shrinkage depth, and (b) Shrinkage overlap depth of six simulation cases.

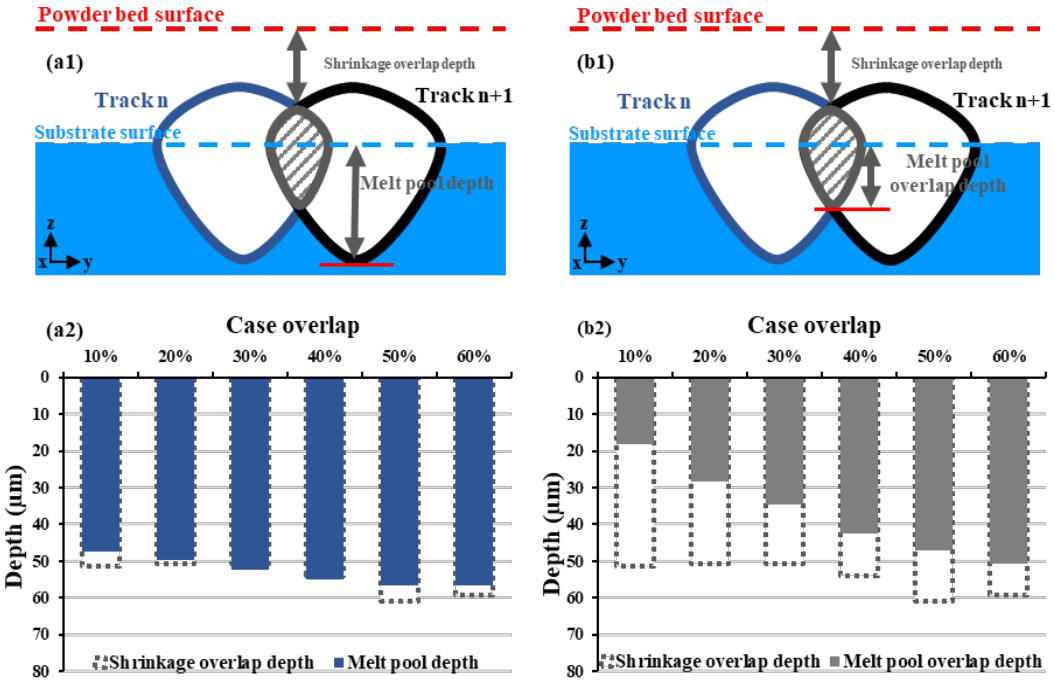

Figure 11. Comparison between: (a1) schematic and data of shrinkage overlap depth and melt pool depth (a2), (b1) schematic and data shrinkage overlap depth and melt pool overlap depth (b2).

While considering the multi-layer SLM process, the depth, and the shrinkage of the melt track of each layer could affect the condition of the built part. In Figure 11(a), the melt pool depths are nearly close to the shrinkage overlap depths in all cases. However, in Figure 11(b), the melt pool overlap depths are less than the shrinkage overlap depths in all cases, especially in the smaller overlap cases, which could create a potential for the lack of fusion defects in the multi-layer melting part. These results could provide supporting information for determining the sufficient energy density and designing scanning strategies to prevent defects during the SLM process.

4. Conclusions

In this study, the impact of overlap percentage on multi-track melting in the Selective Laser Melting (SLM) process for Ti-6Al-4V was investigated through numerical simulations. The results from this study can be contributed as follows:

1. The numerical results closely matched experimental data from Kouprianoff *et al.* on single-track melt pool shape, showing less than 3% differences in width and depth. The model was also applied to this multi-track melting studies.

2. Temperature monitoring with a probe at the third track's center highlighted that overlap percentages crucially influence thermal dynamics, showcasing how previous tracks affect subsequent ones. Specifically, with overlaps of 50% or more, temperatures surpass the liquidus point even before the laser scans the next track, indicating early melting of the forthcoming track due to heat buildup from adjacent tracks.

3. The overlap percentage critically influences melt track surface roughness. Lower overlaps lead to defects from un-melted particles, whereas higher overlaps improve roughness but can result in irregular melt pool shapes. This underscores the need for careful optimization of overlap to achieve both desired surface quality and consistency.

4. Overlaps significantly influence melt pool depth, overlap depth, and shrinkage depth. Lower overlaps result in minor variations in depth values. Conversely, higher overlaps lead to a significant increase in depth due to increased heat accumulation and recoil pressure. Furthermore, the values of overlap and shrinkage depth gradually increase within multi-track melting. These results also affect the quality of the produced parts, as they may contribute to the risk of lack of fusion defects.

The findings of this study provide guidance for fine-tuning SLM process parameters, including refining scanning pattern strategies, and determining the appropriate energy density, to improve the surface roughness, quality and consistency of 3D-printed parts.

Acknowledgements

This research was funded by NSTDA-KMUTNB collaborative research and development of high-quality post graduate scholarship with contract no. Grad012/2564; Thailand science research and innovation fund, and King Mongkut's University of Technology North Bangkok with contract no. KMUTNB-FF-65-48; and National Research Council of Thailand (NRCT) and King Mongkut's University of Technology North Bangkok (KMUTNB) with contract no. N42A650321.

References

[1] D. Dong, C. Chang, H. Wang, X. Yan, W. Ma, M. Liu, S. Deng, J. Gardan, R. Bolot, and H. Liao, "Selective laser melting (SLM) of CX stainless steel: Theoretical calculation, process optimization and strengthening mechanism", *Journal of Materials Science & Technology*, vol. 73, pp. 151-164, 2021.

[2] S. Chowdhury, N. Yadaiah, C. Prakash, S. Ramakrishna, S. Dixit, L. R. Gupta, and D. Buddhi, "Laser powder bed fusion: a state-of-the-art review of the technology, materials, properties & defects, and numerical modelling", *Journal of Materials Research and Technology*, vol. 20, pp. 2109 – 2172, 2022.

[3] M. Bayat, W. Dong, J. Thorborg, A. C. To, and J. H. Hattel, "A review of multi-scale and multi-physics simulations of metal additive manufacturing processes with focus on modeling strategies", *Additive Manufacturing*. vol. 47, 102278, 2021.

[4] M. Bayat, S. Mohanty, and J. H. Hattel, "Multiphysics modelling of lack-of-fusion voids formation and evolution in IN718 made by multi-track/multi-layer L-PBF", *International Journal of Heat and Mass Transfer*. vol. 139, pp. 95-114, 2019.

[5] W. Ge, J. Y. H. Fuh, and S. J. Na, "Numerical modelling of keyhole formation in selective laser melting of Ti6Al4V", *Journal of Manufacturing Processes*, vol. 62, pp. 646–654, 2021.

[6] X. Ao, J. Liu, H. Xia, and Y. Yang, "A numerical study on the mesoscopic characteristics of Ti-6Al-4V by selective laser melting," *Materials*, vol. 15, no. 8, p. 2850, 2022.

[7] W. Wang, and S. Y. Liang, "Prediction of molten pool height, contact angle, and balling occurrence in laser powder bed fusion". *The International Journal of Advanced Manufacturing Technology*, vol. 119, pp. 6193-6202, 2022.

[8] B. Liu, G. Fang, L. Lei, and W. Liu, "Experimental and numerical exploration of defocusing in Laser Powder Bed Fusion (LPBF) as an effective processing parameter", *Optics & Laser Technology*, vol. 149, 2022.

[9] W. Yuan, H. Chen, T. Cheng, and Q. Wei, "Effects of laser scanning speeds on different states of the molten pool during selective laser melting: Simulation and experiment". *Materials & Design*. vol. 189, p. 108542, 2020.

[10] Y. Tian, L. Yang, D. Zhao, Y. Huang, and J. Pan, "Numerical analysis of powder bed generation and single track forming for selective laser melting of SS316L stainless steel". *Journal of Manufacturing Processes*, vol. 58, pp. 964-974, 2020.

[11] M. Zheng, L. Wei, J. Chen, Q. Zhang, G. Zhang, X. Lin, and W. Huang, "On the role of energy input in the surface morphology and microstructure during selective laser melting of Inconel 718 alloy", *Journal of Materials Research and Technology*, vol. 11, 2021.

[12] K. Mahyar, G. AmirHossein, L. Martin, O. William, G. Ian, C. Laura, and R. Bernard, "Numerical and analytical investigation on meltpool temperature of laser-based powder bed fusion of IN718", *International Journal of Heat and Mass Transfer*, vol. 177, 2021.

[13] Z. Wang, W. Yan, W. Liu, and M. Liu, "Powder-scale multi-physics modeling of multi-layer multi-track selective laser

melting with sharp interface capturing method", *Computational Mechanics*, vol. 63, pp. 649-661, 2019.

[14] F. Ali, B. Mohsen, F. Ehsan, and G. Sa'id, "finite element simulation of selective laser melting process considering optical penetration depth of laser in powder bed", *Materials & Design*, vol. 89, pp. 255-263, 2016.

[15] Z. Dong, Y. Liu, W. Wen, J. Ge, and J. Liang, "Effect of hatch spacing on melt pool and as-built quality during selective laser melting of stainless steel: Modeling and experimental approaches", *Materials*, vol. 12, no. 1, pp. 50, 2018.

[16] H. Gu, C. Wei, L. Li, Q. Han, R. Setchi, M. Ryan, and Q. Li, "Multi-physics modelling of molten pool development and track formation in multi-track, multi-layer and multi-material selective laser melting", *International Journal of Heat and Mass Transfer*, vol. 151, 2020.

[17] P. Laakso, T. Riipinen, A. Laukkanen, T. Andersson, A. Jokinen, A. Revuelta, and K. Ruusuvuori, "Optimization and simulation of slm process for high density H13 tool steel parts", *Physics Procedia*, vol. 83, pp. 26-35, 2016.

[18] T. Zakrzewski, J. Kozak, M. Witt, and M. Dębowska-Wąsak, "Dimensional analysis of the effect of SLM parameters on surface roughness and material density", *Procedia CIRP 95*, pp. 115-120, 2020.

[19] Z. Wang, W. Yan, W. K. Liu, M. Liu, "Powder-scale multi-physics modeling of multi-layer multi-track selective laser melting with sharp interface capturing method", *Computational Mechanics*, vol. 63, pp. 649-661, 2019.

[20] M. M. Basha, S. M. Basha, V. K. Jain, and M. R. Sankar, "State of the art on chemical and electrochemical based finishing processes for additive manufactured features", *Additive Manufacturing*, vol. 58, 103028, 2022.

[21] J. Song, Q. Tang, Q. Feng, S. Ma, Q. Han, and R. Setchi, "Effect of remelting process on surface quality and tensile behaviour of a maraging steel manufactured by selective laser melting", *Sustainable Design and Manufacturing (Conference paper)*, pp. 251-260, 2020.

[22] C. Veiga, J. P. Davim, and A. J. R. Loureiro, "Properties and applications of titanium alloys: A brief review", *Reviews on advanced materials science*, vol. 32, pp. 133- 148, 2012.

[23] V. Chastand, P. Quaegebeur, W. Maia, and E. Charkaluk, "Comparative study of fatigue properties of Ti-6Al-4V specimens built by electron beam melting (EBM) and selective laser melting (SLM)", *Materials Characterization*, vol. 143, pp. 76-81, 2018.

[24] C. Bo, L. Xiaobai, T. Charles, I. Alexander, W. Hannes, and H. Udo, "Multi-physics modeling of single track scanning in selective laser melting: powder compaction effect". *Proc. of the 29th Annual International Solid Freeform Fabrication Symposium – An Additive Manufacturing Conference, August 13-15, 2018, Austin, TX, USA, pp. 1887-1902*

[25] X. Shan., Z. Pan., M. Gao., L. Han., J. P. Choi., and H. Zhang., "Multi-physics modeling of melting-solidification characteristics in laser powder bed fusion process of 316L stainless steel", *Materials*, vol. 17, No. 4:946, pp. 1-13, 2024.

[26] W. Wang., W. Lin., R. Yang., Y. Wu., J. Li., Zh. Zhang, and Z. Zhai., "Mesoscopic evolution of molten pool during selective laser melting of superalloy Inconel 738 at elevating preheating temperature", *Materials & Design*, vol. 213, 110355, 2022.

[27] H. Li, X. Liang, Y. Li, and F. Lin, "Performance of high-layer-thickness Ti6Al4V fabricated by electron beam powder bed fusion under different accelerating voltage values," *Materials*, vol. 15, no. 5, pp. 1878, 2022.

[28] P. Ninpetch, P. Chalermkarnnon, and P. Kowitwarangkul, "Multiphysics simulation of thermal-fluid behavior in laser powder bed fusion of H13 Steel: Influence of layer thickness and energy input", *Metals and Materials International*, vol. 29, pp. 536-551, 2023.

[29] Y. Weihao, C. Hui, C. Tan, and W. Qingsong, "Effects of laser scanning speeds on different states of the molten pool during selective laser melting: Simulation and experiment", *Materials & Design*, vol. 189, p. 108542, 2020.

[30] C. H. Fu, and Y. B. Guo, "Three-dimensional temperature gradient mechanism in selective laser melting of Ti-6Al-4V", *ASME. Journal of Manufacturing Science and Engineering*, vol. 136, no. 6, 061004, 2014.

[31] K. C. Mills, "Recommended values of thermophysical properties for selected commercial alloys", *A volume in Woodhead Publishing Series in Metals and Surface Engineering*, pp. 211-217, 2002.

[32] S. B. Umberto,. W. J. Alexander, J. M. Manyalibo, R. De. Jean-Pierre, and M. S. Julie, "On the limitations of volumetric energy density as a design parameter for selective laser melting", *Materials & Design*, vol. 113, pp. 331-340, 2017.

[33] D. Kouprianoff, I. Yadroitsava, A. du Plessis, N. Luwes and I. Yadroitsev, "Monitoring of laser powder bed fusion by acoustic emission: investigation of single tracks and layers", *Frontiers in Mechanical Engineering*, vol. 7, p. 678076, 2021.

[34] D. Chen, G. Li, P. Wang, Z. Zeng, and Y. Tang "Numerical simulation of melt pool size and flow evolution for laser powder bed fusion of powder grade ti6al4v," *Finite Elements in Analysis and Design*, 223, pp. 103971, 2023.